

Spatial and Temporal Variation of Mars South Polar Ice Composition from Spectral Endmember Classification of CRISM Mapping Data

Samuel Cartwright¹, Wendy M. Calvin², Frank Seelos³, and Kimberly D Seelos⁴

¹University of Colorado Boulder

²University of Nevada Reno

³JHU/APL

⁴JHU Applied Physics Laboratory

October 17, 2023

Abstract

Multispectral mapping data from the Compact Reconnaissance Imaging Spectrometer for Mars (CRISM) provide a unique opportunity to characterize south polar ice deposits at higher spectral sampling, spatial resolution, or spatiotemporal coverage than previous work. This new perspective can help to constrain the nature and distribution of different mixtures of CO₂ ice, H₂O ice, and dust that influence the formation, evolution, and preservation of Mars climate records. We processed 1103 CRISM observations spanning southern summer of six Mars Years (MY) through a combination of *k*-means clustering and random forest classification. Using a set of 12 spectral endmembers directly tied to previous work with high-resolution CRISM targeted data, we made a series of temporally restricted mosaics showing surface spectral variation over time. The mosaics show the effects of the MY 28 dust storm on the removal of the seasonal CO₂ ice cap that year and reveal how this process differed from the years that followed. A mosaic showing residual ice surfaces displays broad agreement with previous compositional maps while resolving new details in the distribution of H₂O ice-rich material around the periphery of the bright CO₂ ice cap. By showing how surface composition varies across a broad swath of the south polar region through time, the endmember set and classified mosaics produced in this work can provide critical context for future studies of the dynamic processes that shape south polar ice deposits.

Spatial and Temporal Variation of Mars South Polar Ice Composition from Spectral Endmember Classification of CRISM Mapping Data

S. F. A. Cartwright^{1,2} W. M. Calvin³, F. P. Seelos², and K. D. Seelos²

¹Department of Geological Sciences, Laboratory for Atmospheric and Space Physics, University of Colorado, Boulder, CO, USA

²Johns Hopkins University Applied Physics Laboratory, Laurel, MD, USA

³Department of Geological Sciences and Engineering, University of Nevada, Reno, NV, USA

Corresponding author: Samuel Cartwright (samuel.cartwright@colorado.edu)

Key Points:

- Variable mixtures of CO₂ and H₂O ice with dust are linked to the formation of south polar climate records.
- To better understand these mixtures, we mapped 12 endmembers across multispectral data spanning 6 south polar summers.
- We made a series of mosaics to explore compositional variation in both seasonal and residual ice deposits.

Abstract

Multispectral mapping data from the Compact Reconnaissance Imaging Spectrometer for Mars (CRISM) provide a unique opportunity to characterize south polar ice deposits at higher spectral sampling, spatial resolution, or spatiotemporal coverage than previous work. This new perspective can help to constrain the nature and distribution of different mixtures of CO₂ ice, H₂O ice, and dust that influence the formation, evolution, and preservation of Mars climate records. We processed 1103 CRISM observations spanning southern summer of six Mars Years (MY) through a combination of *k*-means clustering and random forest classification. Using a set of 12 spectral endmembers directly tied to previous work with high-resolution CRISM targeted data, we made a series of temporally restricted mosaics showing surface spectral variation over time. The mosaics show the effects of the MY 28 dust storm on the removal of the seasonal CO₂ ice cap that year and reveal how this process differed from the years that followed. A mosaic showing residual ice surfaces displays broad agreement with previous compositional maps while resolving new details in the distribution of H₂O ice-rich material around the periphery of the bright CO₂ ice cap. By showing how surface composition varies across a broad swath of the south polar region through time, the endmember set and classified mosaics produced in this work can provide critical context for future studies of the dynamic processes that shape south polar ice deposits.

Plain Language Summary

At the south pole of Mars, different mixtures of CO₂ ice, water ice, and dust on the surface influence interactions with the atmosphere. These influences affect how polar ice deposits are formed, how they change over time, and how they are preserved as records of past climates. Existing maps of ice and dust in the region have limitations in how accurately they can describe mixtures and how much detail they can show on the ground. Using data from an orbiting spectrometer that measures sunlight reflected from the surface, we made new maps that reveal important details not seen in previous work. For example, these maps show how surface composition changes through time, which can be used to study CO₂ frost that forms on the surface every winter and is removed in the summer. We observe how a dust storm in one year affected the composition and/or thickness of seasonal frost compared to other years. The maps also reveal how composition varies in different permanent ice deposits. Compared to previous work, it is easier to see how CO₂ ice and dust are mixed with water ice in enigmatic exposures that may be linked to the formation of new climate records.

1 Introduction

Both the present dynamics of Mars's climate and its evolution over the past tens of millions of years are preserved in the icy stratigraphy of the planet's south pole (Byrne, 2009). This has drawn an evergrowing body of observation and related research into the processes that have shaped this fascinating region (Smith, 2022; Landis et al., 2023). A detailed understanding of surface composition is key to interpreting the climate history that these landscapes preserve, specifically how the formation and evolution of ice deposits are influenced by variable mixtures of CO₂ ice, H₂O ice, and settled atmospheric dust. In this paper, we present the first comprehensive study of south polar spectral variation as captured by multispectral mapping data from the Compact Reconnaissance Imaging Spectrometer for Mars (CRISM, Murchie et al.,

2007). We turned to these data for two reasons described below that together provide a unique opportunity to explore connections between south polar ices and the climate history of Mars.

First, CRISM mapping data provide a view of the south polar region that can place the compositional framework outlined by Cartwright et al. (2022) in a broader spatial context. In that paper, we used hyperspectral CRISM data at 18–36 m/pixel to identify and map a set of 21 spectral endmembers at over 100 sites distributed across the south pole. There are two key deposits explored in that work: the ~4 km-thick dome of interbedded water ice and dust known as the South Polar Layered Deposits (SPLD, see Plaut et al., 2007) and the overlying South Polar Residual Cap (SPRC). We further divide the SPRC into the high-albedo Residual CO₂-ice Deposits (RCD, see Thomas et al., 2016) and the moderate-albedo Peripheral Water-ice Deposits and Outlier Water-ice Deposit (PWD and OWD, respectively; see Piqueux et al., 2008). Exposures of these units are labeled in Figure 1 and the reader is referred to Cartwright et al. (2022) for a table with additional unit descriptions.

The endmember classified maps of CRISM targeted data reveal variations in the nature of seasonal CO₂ frost cover (see Prettyman et al., 2009) within and between Mars Years (MYs, Piqueux, Byrne, et al., 2015). In particular, following the large dust event in MY 28 (Calvin et al., 2017; Piqueux, Kleinböhl, et al., 2015), seasonal frost signatures are more persistent within the SPRC compared to other years. In unfrosted residual ice exposures, the classified maps show unexpected complexity in ice mixtures, including CO₂ ice signatures that remain in low-albedo material well into late southern summer. Together these results provide a compelling window into the diversity and dynamism of south polar ice exposures, but this view is ultimately limited by the restricted spatial sampling of high-resolution CRISM maps, which only cover a fraction of the total area of the SPRC. By expanding this work with multispectral CRISM data that offer more complete coverage of these terrains through time, we can assess the accuracy of the existing compositional framework and potentially improve it with new insights.

Second, CRISM mapping data can bridge a gap in understanding between existing maps of south polar composition. While the presence of CO₂ and H₂O ices in the region had been understood for decades (e.g., Kieffer, 1979; Murray et al., 1972) their associations with different surface units were unclear until the arrival of the Observatoire pour la Minéralogie, l'Eau, les Glaces et l'Activité (OMEGA; Bibring, Soufflot, et al., 2004). With 352 spectral channels sampling 0.38–5.1 μm , OMEGA data proved capable of distinguishing varied mixtures of ice and dust across the SPRC and in particular, highlighted the presence of water ice (Bibring, Langevin, et al., 2004; Douté et al., 2007; Langevin et al. 2007). However, the amount of detail captured by these maps is limited by the 700–2000 m/pixel resolution of south polar OMEGA observations. An alternative perspective on Mars surface composition is provided by the Thermal Emission Imaging System (THEMIS; Christensen et al., 2004), which offers a higher spatial resolution of 100 m/pixel. This allowed Titus et al. (2003) to first identify water ice within the SPRC, and later, for Piqueux et al. (2008) to map exposures of water ice more completely. However, with 10 channels covering 6.8–14.9 μm , THEMIS can only identify thermal signatures generally indicative of ice and dust mixtures and cannot characterize them further.

Owing to its spatial resolution of 90–180 m/pixel and spectral sampling of 55 channels in the short-wave infrared (SWIR) from 1.00–3.93 μm , CRISM mapping data can distinguish varied mixtures of CO₂ ice, H₂O ice, and dust with fidelity similar to OMEGA while also resolving their exposure with spatial detail similar to THEMIS. Maps of south polar composition

from CRISM mapping data could therefore bridge the gap between existing views of compositional variation offered by these instruments.

While hyperspectral CRISM data have helped to revolutionize our understanding of Mars surface mineralogy, multispectral mapping data have been comparatively under-utilized. This is especially true in the south polar region, where the last detailed study of these data was only able to cover the first MY of observation (Brown et al., 2010). To address this problem, we have conducted a comprehensive study of CRISM SWIR mapping data at the south pole during the southern summer of each of the 6 MYs for which data were acquired. In this paper, we (a) describe the process of mapping spectral endmembers across the south polar dataset based on those identified in Cartwright et al. (2022), (b) present results from compiling the classified data into a series of temporally restricted mosaics, (c) investigate spatio-temporal trends in the composition of seasonal and residual ice deposits that those mosaics reveal, and (d) discuss how these findings compare to previous work and the broader implications they have for the formation and evolution of south polar ices.

2 Data

2.1 CRISM's Spectral Perspective

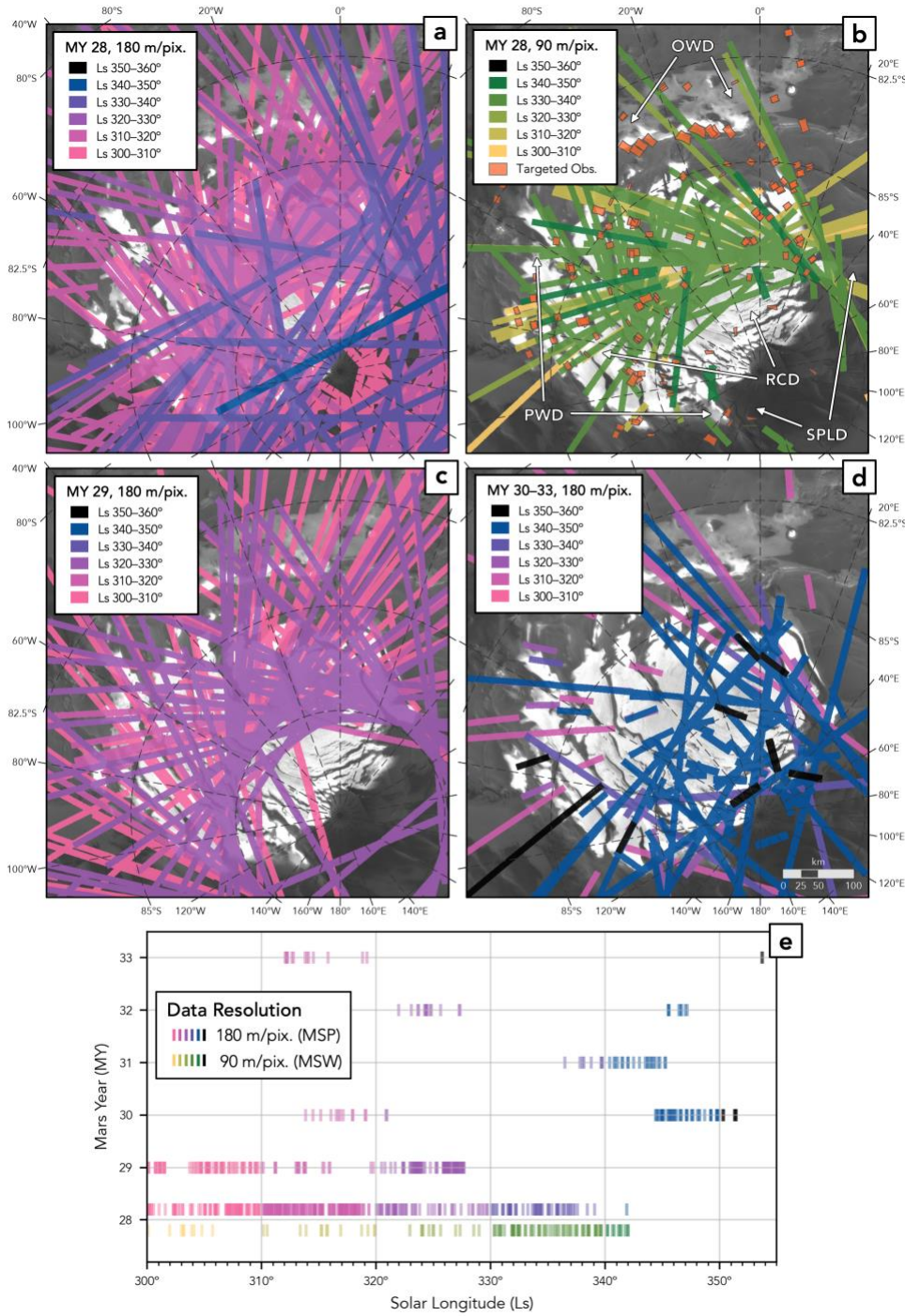
The endmember extraction and mapping presented in Cartwright et al. (2022) leveraged CRISM targeted data, which are observations that rely on the instrument gimbal to point at a specific site on the planet's surface. While these views provide exceptionally high spatial and spectral resolutions (18 or 36 m/pixel, 438 SWIR channels), their footprints are accordingly limited to a maximum area of about 10×20 km. Total coverage of the 167 endmember maps produced in the previous work is therefore only ~5% of the total surface area of ice deposits comprising the SPRC. However, CRISM offers a complimentary dataset in the form of mapping data, which are acquired in pushbroom configuration to image broad swaths of the surface. These data trade larger areas (10×500+ km) for more limited spatial and spectral sampling (90 or 180 m/pix, 55 or 154 SWIR bands). These qualities enable CRISM mapping data to be compiled into mosaics that show spectral variation at regional scales (Viviano et al., 2020; Seelos et al., 2023), which in turn makes it possible to fill gaps in understanding left by previous compositional maps.

There are two observing modes of CRISM mapping data relevant to this study which share a spectral sampling of 55 SWIR channels (sufficient to capture key CO₂ and H₂O ice absorption features), but differ in spatial resolutions and temporal sampling (Fig. 1). Multispectral Survey (MSP) observations show the surface at 180 m/pixel resolution and were acquired throughout the same period as targeted SWIR observations (MY 28–33). When taken in aggregate, MSP data provide nearly universal coverage of the RCD during southern summer. The temporal sampling of Multispectral Window (MSW) data is comparatively limited in that it only captures the southern summer of MY 28, which in turn leads to less comprehensive spatial coverage. However, MSW mapping strips image the surface at 90 m/pixel, which allows them to resolve details around large erosional mesas on the surface of the RCD and narrow exposures along its margins.

2.2 Data Coverage and Temporal Sampling

To capture spatial variation in and around the SPRC, we ran endmember processing on all MSP and MSW strips that cover the region below 81°S and between -135–60°E. We restricted

147 this set to only observations that span from southern summer solstice to southern autumnal
148 equinox, which corresponds to an aerocentric solar longitude (L_s) of 270–360°. We did not place
149 any restrictions on the local time of acquisition for the data, which span from ~14:00–2:00.
150 Spatial and temporal trends in the final set of 983 MSP and 120 MSW observations are
151 illustrated in [Figure 1](#). The greatest density of coverage was acquired in MY 28 and 29
152 (particularly with MSP data) and almost any temporal slice through the dataset greatly expands
153 on the corresponding coverage offered by targeted data observations. However, it is important to
154 note that spatial and temporal coverage (in terms of sampled L_s) varies significantly between
155 MYs, with particularly sparse coverage from MY 30–33. This means that the most effective
156 inter-annual comparisons can be made between MY 28 and 29, though some L_s ranges offer
157 opportunities to compare up to four MYs.



158

Figure 1. Spatial and temporal coverage of south polar CRISM mapping data used in this study. Observations that fall within 10° bins of solar longitude (Ls) are rendered with the same color while two color gradients are used to differentiate observing modes and their associated spatial resolutions: pink-blue for Multispectral Survey (MSP, 180 m/pixel) and yellow-green for Multispectral Window (MSW, 90 m/pixel). Note that while our analyses span Ls >270°, only Ls >300° are presented here for clarity. (a) MSP coverage in Mars Year (MY) 28. (b) MSW coverage in MY 28 and footprints of CRISM targeted data used in [Cartwright et al. \(2022\)](#) that span Ls 300–360° in MY 28–33. Labels note exposures of the key ice deposits described in the

text: high albedo Residual CO₂-ice Deposits (RCD), moderate albedo Peripheral Water-ice Deposits (PWD) and Outlier Water-ice Deposit (OWD), and low albedo South Polar Layered Deposits (SPLD). (c) MSP coverage in MY 29. (d) MSP coverage across MY 30–33. (e) Plot of temporal sampling in which each tick is a single observation, colored according to L_s bin and plotted by the MY and L_s at which it was acquired. A vertical offset is used to separate the two observing modes in MY 28 while a slight transparency highlights times of denser coverage.

2.3 Data Processing and Reduction

Pre-processing of the data used in this study was based on a new workflow developed for the creation of next-generation CRISM map mosaic products (Seelos et al., 2023). While the pipeline is designed to use a network of radiometrically calibrated reference strips to reconcile differences between data, this reference network is not available at the poles. We therefore chose to focus solely on the strip-independent processing steps that are part of this workflow and which are based on corresponding state-of-the-art corrections used to generate CRISM Targeted Empirical Records (TERs). In this portion of the workflow, each mapping data strip is passed through ratio shift, photometric, atmospheric, and spectral smile corrections to produce the clearest possible view of surface spectral variation. The reader is referred to Murchie et al. (2016) for additional details on each of these corrections.

The map-projected data were then converted to *numpy* arrays for endmember analyses. This process included filtering each spectrum to remove and interpolate across bad bands; four channels around the SWIR filter boundary and longest wavelengths had consistently suspect radiometry and were removed. The spectra were then normalized by the reflectance measured at 1.330 μm (the R1330 parameter described in Viviano-Beck et al., 2014); this method differs slightly from our work with targeted observations due to the more limited spectral sampling of mapping data.

3 Methods

3.1 Machine learning methods in previous work

The spectral endmembers and classified maps presented in Cartwright et al. (2022) were produced by applying versatile machine learning algorithms to CRISM targeted data. First, a set of candidate endmembers were identified from a subset of high-quality, representative observations using *k*-means clustering. This is an unsupervised learning technique that divides a set of *n* samples (e.g., CRISM spectra) into *k* clusters such that the variance between samples within each cluster is minimized (Arthur & Vassilvitskii, 2007). Those candidate endmembers were then mapped across the entire dataset using random forest classification. This is an ensemble learning method in which a large number of decision trees independently evaluate the features of a sample (e.g., a CRISM spectrum) and vote to assign it a classification (Breiman, 2001). These two methods proved useful in distilling compositional information from a large spectral dataset and yielded tightly constrained endmembers with spatially consistent classified maps. We therefore chose to leverage these tools again in expanding the work to CRISM mapping data. The reader is referred to Cartwright et al. (2022) for additional detail on the model parameters associated with these two methods and their implementations in the context of hyperspectral image data.

3.2 Initial classification attempt

The most straightforward approach to expanding on this work is to directly map the previously derived targeted data endmembers onto mapping data spectra. To do this, the training data used to build the original random forest model are simply subsampled from their native 438 SWIR channels to the set of 55 channels that are also sampled by MSP and MSW data. A new random forest model can then be trained with these spectra and used to classify individual pixels from mapping data strips. In practice, however, we found that this method produces two main types of misclassification: 1) along-track striping that indicates subsampled targeted data spectra do not capture noise unique to mapping data, and 2) inconsistent mapping of some water ice-rich endmembers that suggest the weaker CO₂ absorptions used to distinguish them are not captured by the random forest model.

3.3 New classification workflow

To address these misclassification issues, we developed a new workflow (Fig. 2) to generate the results presented in this paper. The key difference is that this workflow incorporates mapping data and its unique characteristics from the start to build a set of candidate endmembers which are then used as training data for the random forest classification model. We then correlate the mapping data-derived endmembers to the spectral features and surface expression of those derived from targeted data.

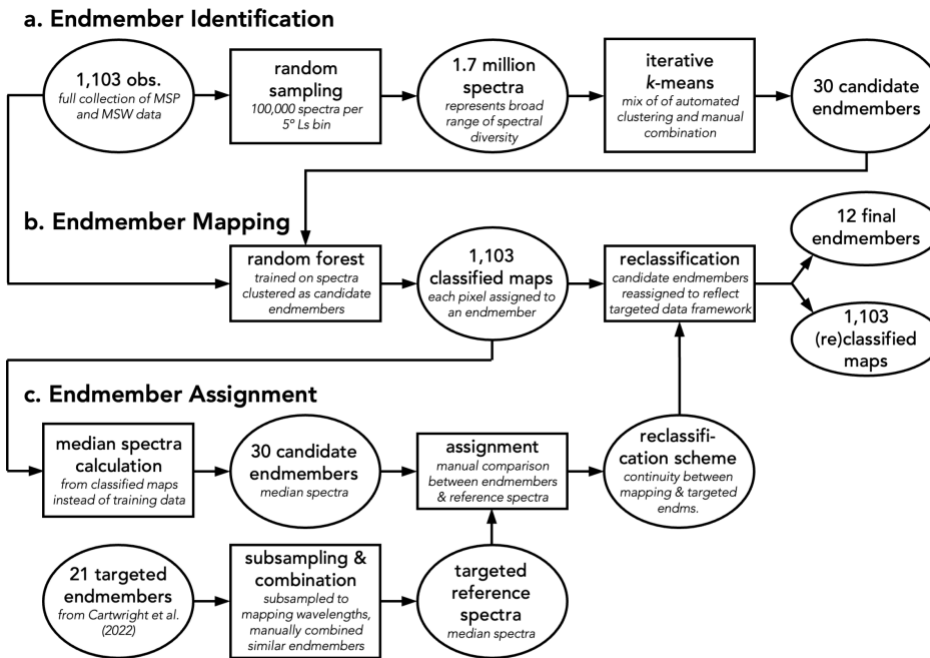


Figure 2. Workflow diagram of the methods used to (a) extract a set of candidate endmembers unique to south polar mapping data from CRISM, (b) map those endmembers across each

observation in the dataset, and (c) assign those endmembers to an appropriate reference spectrum derived from south polar CRISM targeted data presented in [Cartwright et al. \(2022\)](#).

3.3.1 Endmember identification with k -means clustering

To increase the efficiency of the k -means clustering procedure, we reduced the mapping dataset to a representative sampling. This was done by moving sequentially in 5° L_s bins between L_s 270–360°, making compilations of all the MSP and MSW observations acquired within each bin, and randomly sampling 10^5 pixels from each compilation. By aggregating the samples for each bin in which data were collected, we built a collection of 1.7 million spectra (equivalent to $\sim 1\%$ of the full dataset). This compilation offers a broad sampling of south polar terrains, but without the temporal sampling bias inherent in the south polar mapping dataset ([Fig. 1e](#)).

To avoid clustering results that were driven to local minima by unfiltered bad bands (see data filtering outlined in [Section 2.3](#)), we truncated the pixel compilation to remove all spectral channels at wavelengths longer than $2.6\ \mu\text{m}$. An iterative process of k -means clustering was then applied in which an initial set of 10 clusters were generated, their mean spectra were manually evaluated, and similar clusters were combined. Spectra assigned to each of the new, combined clusters were divided again by the k -means algorithm and evaluated. This process was repeated until all clusters could be distinguished by meaningful spectral differences, resulting in a set of 30 candidate endmembers ([Fig. 2a](#)). Despite the separability of the spectra in this set, it was understood that subsequent processing would necessarily reduce this to a collection of final endmembers no larger than the 21 identified with targeted data.

3.3.2 Endmember mapping with random forest

We trained the new mapping data-derived random forest model with a set of 1,500 randomly sampled spectra from each of the 30 candidate endmembers. We found that a forest with $n_{\text{tree}} = 1,000$ and $m_{\text{try}} = 10$ was able to reduce the reported out-of-bag (OOB) error to 8.5%. The trained model was used to classify each of the ~ 17 million pixels across the collection of 1,103 MSP and MSW observations ([Fig. 2b](#)). Median spectra were then calculated for each of the 30 candidate endmembers that had been mapped.

3.3.3 Endmember correlation

The final step in the classification workflow was to assign each of the candidate mapping data endmembers to the most similar endmember derived from the targeted dataset, allowing for a one-to-one comparison of the results from the two investigations ([Fig. 2c](#)). First, the targeted data endmembers were downsampled to mapping data wavelengths to make a set of reference spectra. Then the strengths and combinations of absorption features in each of the 30 candidate endmembers were compared visually to the features present in the reference spectra. Candidate endmembers were then assigned to the best overall match to their spectral structure; additional details on this comparison process are presented in [Supporting Information S1](#). The resulting reclassification scheme was used to reassign the random forest classification of each mapping data pixel to fit the compositional framework developed with targeted data. [Lastly](#), a collection of 10^4 randomly sampled spectra were pulled for each of the endmembers to calculate the median spectrum along with other percentile statistics characterizing the degree of spectral variation.

3.4 Mosaic creation

To assess temporal changes within and between MYs, we generated a series of mosaics for 10° L_s bins across six southern summers. Mosaics were made by stacking endmember-classified mapping strips in ascending order of L_s; no manual editing, reconciliation of classification results between strips, or geodetic control were applied. Each product was exported at 180 m/pixel and in MY 28, combined MSP and MSW observations. Using these temporally restricted mosaics, we identified the L_s ranges in each MY that did not show endmembers associated with seasonal CO₂ frost. Mapping strips from those ranges were then compiled to generate a final mosaic that primarily shows residual ice. The mosaics were evaluated in GIS software in comparison to other remote sensing datasets like THEMIS and OMEGA compositional maps and a mosaic of Context Camera (CTX) data (Douté et al., 2007; Piqueux et al., 2008; Thomas et al., 2016).

4 Results

4.1 Endmember spectral characteristics

Endmembers in the Cartwright et al. (2022) framework span a wide range of apparent mixtures of ice and dust present at the south pole. To effectively show this variation, the endmembers were sorted by compositional gradients and each was named with an alphanumeric code indicating relative strengths of features associated with CO₂ ice (C/c), water ice (W/w), and dust (D/d). For example, Dc1 represents a spectrum dominated by dust signatures but with secondary CO₂ ice features. Numbers and color gradients indicate gradation towards the strength of a third component; for example, Dc3 displays stronger contributions from water ice than Dc1. The set of 12 endmembers now identified in mapping data inherits the colors and names used in the previous set, but with an appended “m” to indicate association with CRISM mapping data (e.g., Dc3m). Although not every one of the 21 targeted endmembers has an equivalent in the new set, the mapping data capture a similarly broad sampling of ice and dust mixtures.

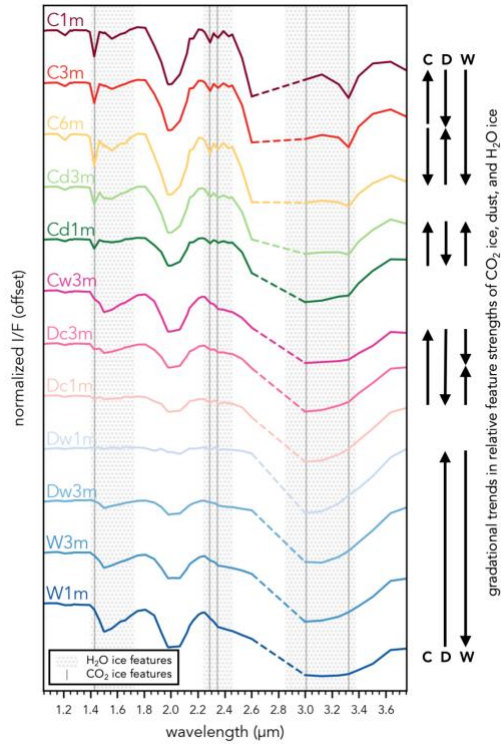


Figure 3. Median spectra of each endmember mapped across the multispectral mapping dataset with random forest classification. Dashed portions of spectra represent interpolation across the CRISM filter boundary. Arrows to the right of the plot indicate trends towards increasing feature strength for CO₂ ice, dust, and water ice.

The 12-endmember set (Fig. 3) includes a pure CO₂ ice spectrum (C1m, deep red) that grades towards increasing water ice contribution (C3m, red and C6m, yellow) evidenced by a strengthening of the 1.5 μm feature and suppression of albedo around 3.1 μm . As in the previous work, we found that this group of endmembers is closely associated with seasonal CO₂ frost (C1m) and residual CO₂ ice with likely sub-pixel contributions from water ice around erosional features (C6m). Also found in the set is a pure water ice spectrum (W1m, deep blue) that grades towards a nearly pure dust spectrum (Dw1m, pale blue). These endmembers are known to be associated with portions of the PDW/OWD and the SPLD, respectively. Other endmembers (shades of pink) indicate a more complex interplay of these mixing components in which a relatively weak but constant CO₂ ice absorption is found with dust (Dc1m), water ice (Cw3m), or an intermediate combination (Dc3m). Transitioning towards stronger CO₂ ice features (shades of green), other endmembers are similarly split between stronger dust (Cd1m) and water ice (Cd3m). Targeted data showed these pink and green endmembers to be associated with a wide variety of terrains around the SPRC and across Ls.

The only spectral type in this broad sampling that is apparently absent from the mapping data is one with exceptionally strong absorption features associated with both CO₂ ice and water ice. In targeted data, this endmember (Cw1) was found to be closely associated with the removal of seasonal frost over water ice-rich terrain. It is likely that either the narrow Ls range in which this late-stage removal occurs is not well sampled by the mapping dataset or that coarser spatial and spectral sampling are insufficient to adequately capture the phenomenon.

In comparison to spectra from targeted data endmembers, these mapping data endmembers have *stronger* CO₂ ice features in CO₂ ice-dominated spectra, but *weaker* H₂O ice features in H₂O ice-dominated spectra (see [Fig. S3](#) in Supporting Information S1). Other trends are at play in mixtures, but most notably, Cw and Dc endmembers (shades of pink) have weaker CO₂ ice absorptions in mapping data. These trends point to potential differences in how ice on the surface is captured by CRISM mapping data and/or interpreted by our endmember extraction and mapping methods.

4.2 Temporal trends

Given its spatial and temporal coverage, the south polar mapping dataset captures a highly detailed view of how the planet's surface has changed across Ls and between MYs. One way to distill this wealth of information is through proportional bar plots like those shown in [Figure 4](#). Here, all observations falling in 10° Ls bins were compiled and the mapped areas of each endmember in each observation were calculated. It is important to keep in mind that trends in CRISM's spatial and temporal sampling can limit the overall area and terrains covered in each Ls bin, and therefore, exact areas or individual Ls bins should not be over-interpreted. However, these plots do effectively illustrate broader temporal trends in surface composition by showing the relative proportions of each endmember mapped in temporal slices.

Dc3m) than light pink (Dc1m), more light green (Cd3m) compared to dark green (Cd1m), and a greater proportion of yellow (C6m) rather than dark red (C1m). This trend is true for both MY 28 and for the years that followed, but there is also a notable difference seen between these temporal slices. Endmembers with stronger CO₂ ice features (deeper reds of C1m, C3m) are prevalent in MY 28 and there is not a significant proportion of area mapped with slight H₂O ice absorptions (yellow of C6m) until late in the summer. In contrast, subsequent years (MY 29–33) show that C6m is mapped in greater proportions than C1m/C3m across Ls.

These results are in agreement with those presented in [Cartwright et al. \(2022\)](#), but also expand on these temporal trends. In addition to greatly increasing the surface area imaged in each Ls range, the mapping data also expand on the previous Ls 300° cutoff and show spectral variation from Ls 270° onward. This reveals that although south polar terrains at Ls 340–350° in MY 28 had similar endmember expressions to those during Ls 320–330° in the years that followed, this does not represent a simple temporal offset of endmember regime. In other words, the endmember expression seen in MY 28 is not simply shifted back to earlier Ls in subsequent years; there is instead a fundamental difference in how CO₂ ice-rich endmembers are expressed at the surface.

4.3 Residual ice mosaic.

To produce a consistent view of residual ice, we evaluated the temporal extent of endmember C1m (deep red) in [Figure 4](#) and its spatial extent in temporally restricted mosaics. This constrained the Ls cutoff in each year after which there does not appear to be significant seasonal frost on the surface, corresponding to Ls 338° in MY 28, Ls 320° in MY 29, and Ls 310° in MY 30–33; all observations from MY 32 were also cut to remove anomalous mapping of H₂O ice-rich endmembers (likely related to atmospheric conditions). The resulting 180 m/pixel mosaic of MSP and MSW data ([Fig. 5](#)) covers ~ 90% of the bright RCD deposits and significant portions of the surrounding PWD and OWD. In this mosaic, the RCD is dominated by a spectral signature of CO₂ ice with weak H₂O ice absorptions (endmember C6m, yellow), though some areas show increased H₂O contributions (Cd3m, pale green). This is consistent with late-summer targeted data from [Cartwright et al. \(2022\)](#) and suggests that even at the coarser resolution of mapping data, sub-pixel contributions from water ice around erosional mesas and other features in the RCD are still visible. However, while targeted data endmember maps had shown ubiquitous expression of CO₂ ice absorptions extending several km beyond the bright exposures of the RCD, expression of these endmembers (pinks of Cw and Dc) are not mapped as consistently between classified mapping strips.

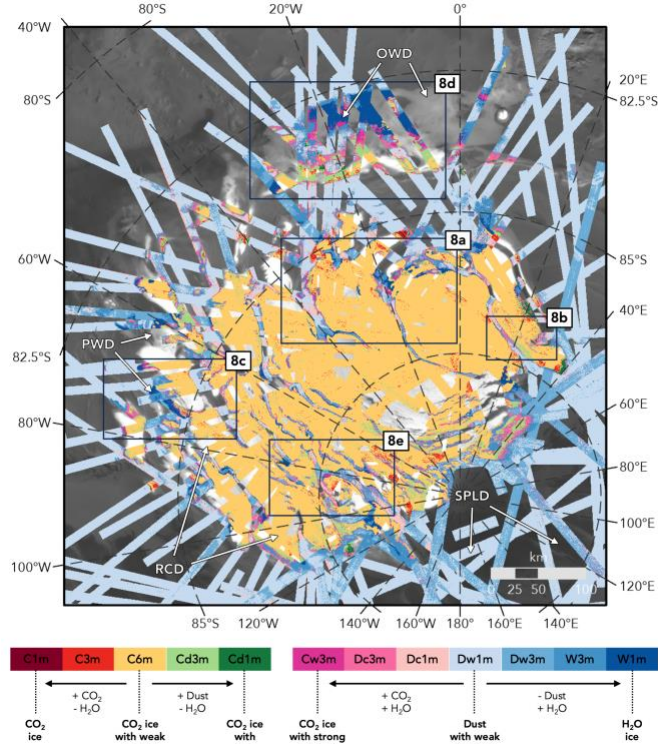


Figure 5. Mosaic showing residual ice exposures with minimal influence from seasonal CO₂ frost. Classified mapping data strips are stacked in ascending order of L_s and compiled from all data acquired after L_s 338° in MY 28, L_s 320° in MY 29, and L_s 310° in MYs 30, 31, and 33. Note the strong agreement between endmember contacts in the mosaic and albedo variations seen in the basemap. Extent indicators are shown for panels in Figure 8.

4.4 Errors and constraints

To constrain how consistently and accurately the random forest classification worked on the mapping dataset, we calculated the spectral variation within each endmember. These statistical envelopes (see Section 3.3.3) include the median spectrum as well as the middle 50% and middle 80% of values at each wavelength. Across endmembers and at the majority of wavelengths, the middle 50% of values are within $\pm 3\%$ of the median and the middle 80% of values are within $\pm 8\%$. We are therefore confident in the endmember classifications given by the random forest model. In terms of spatial expression, endmember classifications in similarly-timed overlapping observations are in close agreement, meaning that mosaics of narrow L_s ranges show consistent mapping of endmembers across the surface. However, as L_s ranges are expanded or data are aggregated across MYs, there is much greater strip-to-strip variation in endmember expression.

5 Discussion

5.1 Temporal variation

Analyses of CRISM targeted data in [Cartwright et al. \(2022\)](#) revealed several temporal trends in the surface expression of endmembers, the most striking of which being a dominance of CO₂ ice-rich endmembers without H₂O ice contribution across L_s in MY 28 compared to the years that followed. This result was unexpected given that previous studies of thermal and visible data demonstrated that the seasonal CO₂ ice cap had experienced an accelerated retreat following the globe-encircling dust event that occurred during $265^{\circ} < L_s < 325^{\circ}$ of MY 28 ([Calvin et al., 2017](#); [Piqueux, Kleinböhl, et al., 2015](#)). If that enhanced retreat were assumed to continue into the interior of the RCD, we would expect to see the addition of weak water ice signatures associated with underlying residual ice revealed at earlier L_s. To instead see sustained CO₂ ice signatures without H₂O ice contribution in the RCD compared to MY 29–33 suggests that these bright CO₂ ice deposits actually experienced a thicker, more prolonged, or otherwise anomalous seasonal cover following the dust event of MY 28. Results from the new mapping data analyses support this story ([Fig. 4](#)), but the expanded spatial and temporal coverage offered by the dataset also provides additional context and complexity.

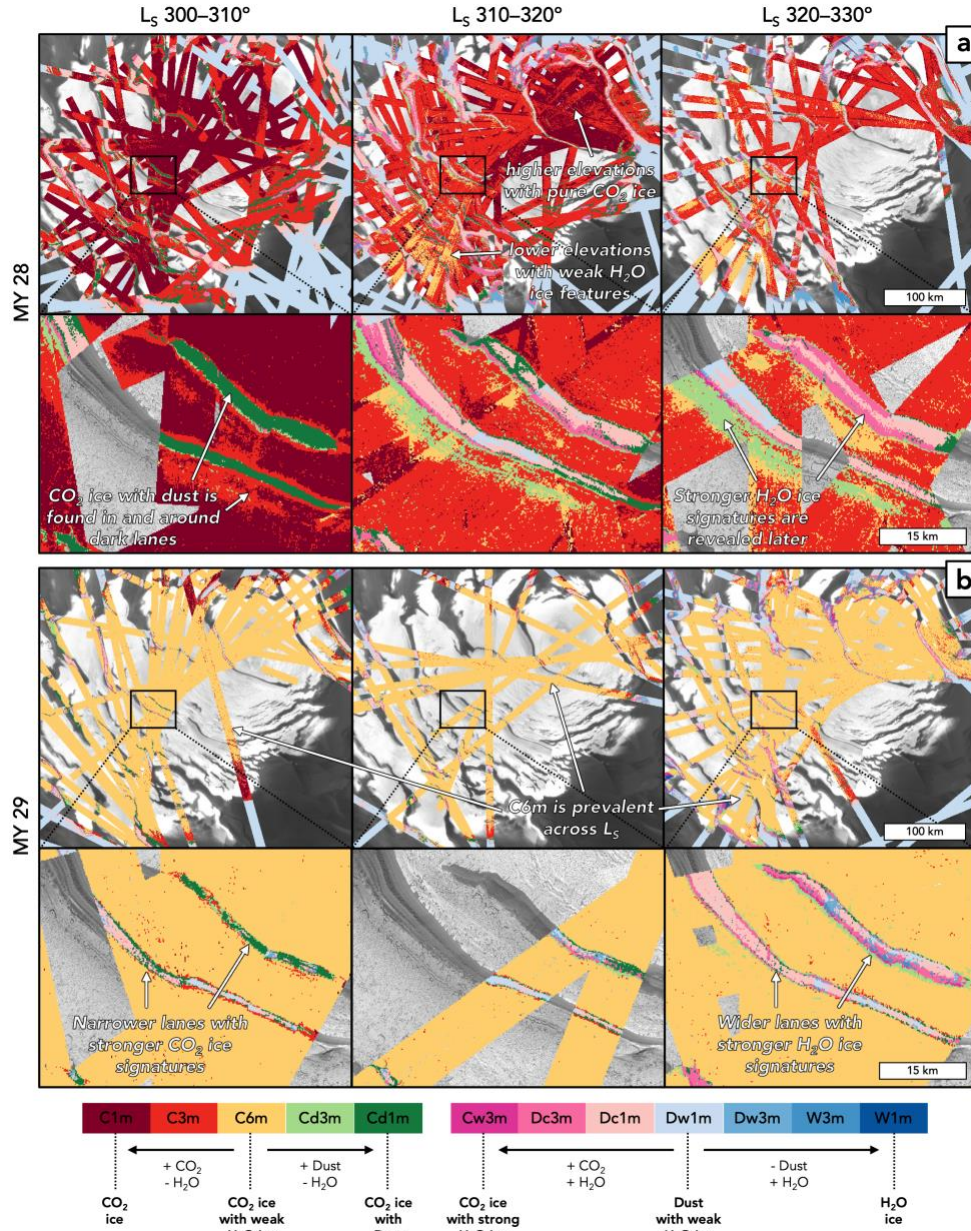
5.1.1 Early southern summer

The mapping data show that the differences in endmember expression between MY 28 and MY29–33 began earlier than the L_s 300° cutoff explored in targeted data and extend at least to the start of southern summer at L_s 270° (Section 4.2; [Fig. 4](#)). This finding suggests that the MY 28 dust event did not simply cause a delay in the retreat of seasonal frost from the surface of the SPRC, but instead fundamentally changed the nature of its deposition/removal. It is unclear whether the MY 28 seasonal frost was anomalous because deposition of a thicker frost cover obscured underlying water ice, or because the frost itself did not bear the same water ice contribution seen in other years.

5.1.2 Spatial variation of frost signatures

While the simplified bar plots effectively illustrate seasonal changes in endmember occurrence, the full temporally restricted mosaics are able to show how these changes are expressed spatially. In particular, these mosaics show variations in the retreat of seasonal frost across the SPRC at different times, both within and between MYs ([Fig. 6](#)). For example, mosaics from MY 28 display when and where transitions occur from the purest CO₂ ice endmember without significant H₂O ice contribution (deep red C1m) to CO₂ ice-rich endmembers with greater H₂O ice signatures (yellow C6m, green Cd3m). These endmember transitions are most visible at L_s 310–320° where the full breadth of seasonal frost removal can be seen in association with different parts of the SPRC ([Fig. 6a](#)). Of particular note are lower elevations of the topographic dome that show extensive exposure of C6m (yellow) and higher elevations where C1m (deep red) is more prevalent. There are even variations in endmember expression on either side of low albedo troughs and slopes that divide RCD exposures (known as dark lanes; e.g., [Thomas et al., 2000](#)). These findings are again consistent with the CRISM targeted data maps, but reveal that seasonal frost re-deposition and removal in MY 28 was more complex than previously understood. Specifically, the thickness or longevity of the seasonal cover appears to be influenced by differences in elevation or illumination such that lower elevations experience earlier removal. Alternatively, stronger water ice signatures in some areas could be linked to

445 local re-deposition of H₂O sublimated from dark lanes (Diniaga et al, 2021; Titus et al., 2020). In
 446 either case, these compositional variations have important implications for how dust storms and
 447 other dynamic processes might affect the mass balance of the RCD and the evolution of south
 448 polar topography more broadly.



449 **Figure 6.** Views of temporally restricted mosaics of classified CRISM mapping data presented in
 450 10° Ls bins over two MYs. (a) Endmember progression across MY 28 that shows spatial
 451 variations in the exposure of more water ice-rich endmembers over time, likely caused by the
 452 removal of seasonal CO₂ frost. (b) Variations over the same Ls bins in MY 29 which display a
 453

very different endmember progression dominated by C6m, a CO₂ ice spectrum with minor contribution from water ice. Insets in both panels show details of the mosaics near dark lanes.

5.1.3 Water ice signatures after MY 28

The corresponding L_s-binned mosaics from MY 29 (Fig. 6b) show a very different evolution in endmember expression. Across L_s, the surface of the RCD is dominated by C6m (yellow) while the C1m endmember (deep red) that dominates much of MY 28 is relatively absent. This matches the trends shown in the bar plots in Figure 4 and suggests that there is weak, but consistent contribution from water ice to CO₂ spectra from L_s 270° onwards in MY 29, as well as in the limited windows CRISM sampled in MY 30–33. This is unexpected given that seasonal frost, which previous work has shown to persist until L_s ~330° (Calvin et al., 2017; James et al., 2007; Piqueux, Kleinböhl, et al., 2015), is assumed to have a different spectral signature from underlying residual ice. Instead, frosted and unfrosted surfaces in the endmember maps appear to have identical compositions of CO₂ ice with minor contribution from H₂O.

However, it is important to note that of the 30 candidate mapping data endmembers, six were reclassified to map as C6m. Spectral features within this group do show some variation, but critically, they all display spectral structure around 1.5 μm and a negative slope at ~2.3 μm consistent with the C6 endmember identified in targeted data. And more importantly, these features readily distinguish the C6m spectra from the candidate endmembers reclassified to C1m and C3m (see Fig. S2b in Supporting Information S1). This suggests that there may be a progression from weaker to stronger H₂O ice features in MY 28 captured by the candidate endmembers, but that this progression is subtle enough to not be captured by the simplified 12-endmember set.

There are some notable exposures visible in the MY 29 mosaics that provide additional context to the C6m signature. First, C6m signatures are seen to extend beyond the bounds of the bright residual CO₂ ice at its outer margins and into parts of low-albedo dark lanes, making them appear narrower in classified maps (Fig. 6b). Second, in areas not mapped as C6m such as the interiors of dark lanes, an endmember progression echoing targeted data maps is found: more CO₂ ice- and dust-rich endmembers (shades of green) transition to spectral shapes with weaker CO₂ features (shades of pink) as the summer progresses. Both of these findings confirm that seasonal frost and its removal are being observed in these mosaics. Specifically, the retreat of the seasonal cap can be tracked in areas near the RCD margins unlike in MY 28, where seasonal ice signatures are coincident with the RCD from early on in the summer.

There is existing evidence that seasonal frost may carry a measurable signature of H₂O ice. The north polar seasonal cap has been observed through a variety of thermal and spectral data to have an annulus of water ice as it retreats (Wagstaff et al., 2008; Appéré et al., 2011; Brown et al., 2012). At the south pole, previous work with OMEGA data has shown that “H₂O contamination” of CO₂ frost fluctuates across L_s as the seasonal cap retreats (Langenvin et al., 2007) while Mars Climate Sounder data show that CO₂ snowfall can scavenge H₂O from the atmosphere (Alsaeed & Hayne, 2022). While it is possible that the lack of H₂O ice signatures in MY 28 frost points to a thicker seasonal cap that obscured water contributions in underlying residual ice exposures, the new findings suggest that H₂O usually present in the seasonal cap may have been kept in the atmosphere with dust from the MY 28 storm.

5.2 Residual ice mosaic

5.2.1 Connections to previous work

The mosaic of CRISM mapping observations showing residual ice signatures offers important new context to previous maps of south polar composition (Fig. 7). This view greatly expands on the coverage offered by targeted data maps from Cartwright et al. (2022)(Fig. 7a), which allows the compositional framework presented in that work to be evaluated across an even more diverse set of SPRC terrains. The broadened framework also serves to bridge gaps in understanding between previous THEMIS and OMEGA-derived maps and provide a more comprehensive view than previously possible of the processes that drive the formation and evolution of south polar ices.

Douté et al. (2007) leveraged four OMEGA images covering L_S 335–348° in MY 26 to produce the first comprehensive view of south polar spectral diversity. They used radiative transfer modeling of pixels to separate spectral types in a ternary diagram of CO₂ ice, H₂O ice, and dust content. One of the derived compositional maps is presented in Figure 7c along with a legend that roughly correlates the feature strengths indicated by their model results to the variations observed in CRISM mapping data endmembers. While the dust-to-water-ice transition and expression of residual CO₂ ice are in close agreement between the two datasets (see the interior of the RCD and vast exposures of the SPLD), other spectral types are more difficult to correlate. These compositions are found primarily around the margins of the RCD and in narrow exposures that extend onto the SPLD, further demonstrating that these are some of the most complex and varied ice mixtures in the region. The enhanced spatial resolution of 180 m/pixel offered by CRISM mapping data compared to the ~2 km/pixel provided by OMEGA allows greater detail of compositional variation to be observed in these places. Meanwhile, the increased temporal sampling over several MYs helps to assess which characteristics of the exposures remain constant through time.

A highly detailed map of THEMIS thermal signatures was made by Piqueux et al. (2008) and for the first time mapped the full extent of the OWD. Measured temperatures were used to characterize areas that contain significant CO₂ ice, areas where H₂O ice dominates, and areas with intermediate temperatures indicating some type of mixture. The 100 m/pixel resolution of THEMIS is comparable to the CRISM mosaic and there is very strong agreement between the two datasets in terms of dominant surface composition (Fig. 7d). This is even the case in relatively small and isolated patches of H₂O ice that sit farther from the RCD margins. The CRISM data help to complete this picture by mapping within the THEMIS coverage gap below 87° S, but more importantly, provide new details in spectral variation, particularly in water ice-rich exposures. For example, the amount of dust contributing to different parts of the PWD can be assessed and areas that show more pure water ice can be clearly identified. Additionally, the most extensive areas mapped as generic mixtures by Piqueux et al. (2008) in the OWD are revealed as CO₂ ice with stronger water ice signatures than typical residual cap exposures (shades of green from Cd3m rather than yellow of C6m). These variations indicate that the isolated patches of CO₂ ice that sit atop the OWD are different from the main RCD exposures that sit at higher elevations.

In summary, these three compositional maps have broad agreement in the distribution of basic compositional mixtures. This is clearest in the interior of the RCD, but also extends to the surrounding PWD, where the improved spectral and spatial resolution of CRISM mapping data is

particularly adept at showing the diversity of H₂O ice mixtures with dust and/or CO₂ ice. There is less agreement in the OWD, though this is likely linked to this region’s pronounced inter-annual variability in CO₂ frost cover (e.g., Calvin et al. 2017) and the limited ability to make one-to-one comparisons between units/endmembers in the three maps.

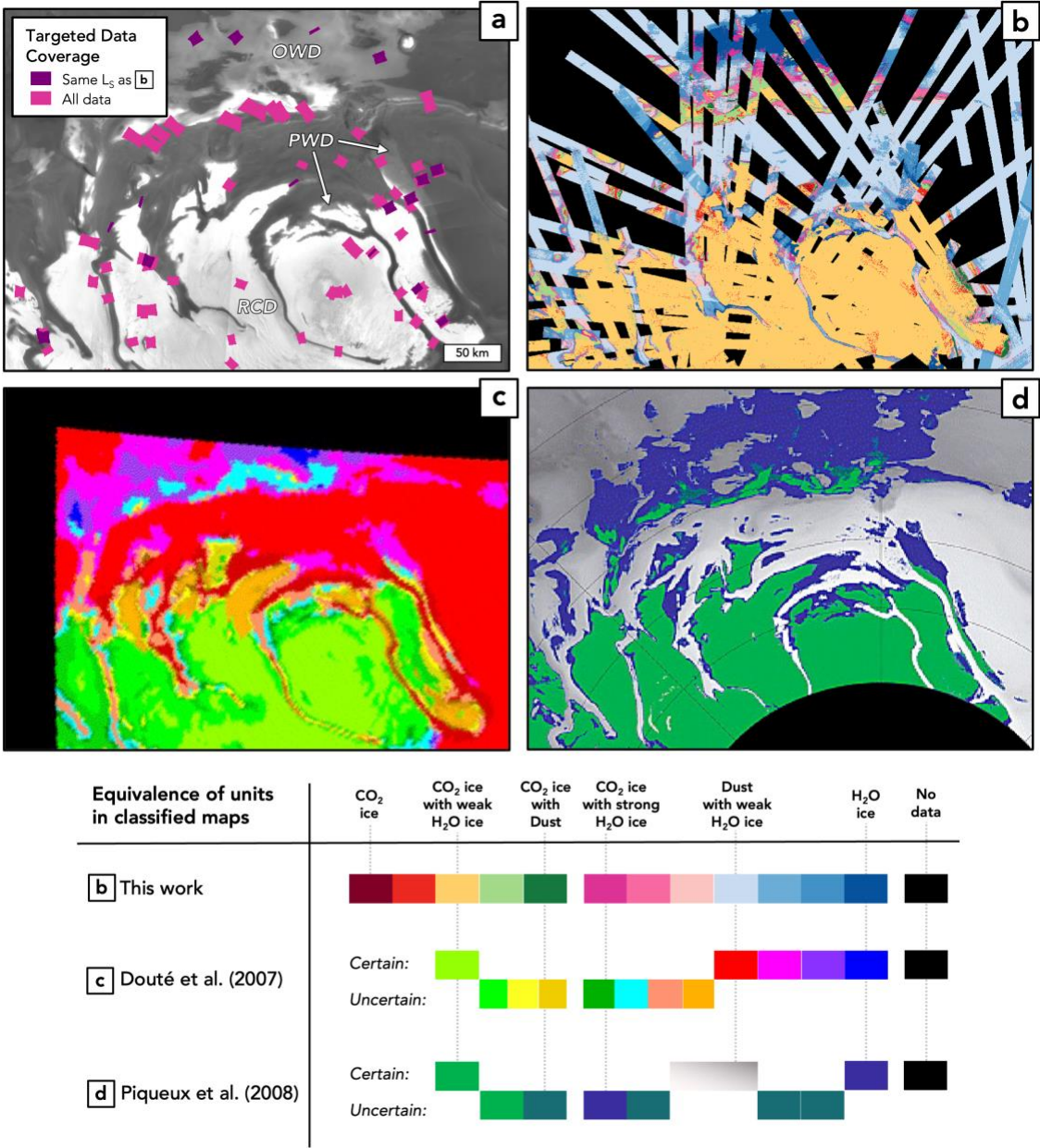


Figure 7. Comparisons of compositional maps of the south polar region. (a) Coverage from classified maps of CRISM targeted data from Cartwright et al. (2022) showing all observations vs. those that cover only the same MY and L_s ranges as the mapping data mosaic. (b) Mosaic of endmember-classified CRISM mapping data showing exposures of residual ice (i.e., not significantly obscured by seasonal CO₂ frost). (c) Classified image from Douté et al. (2007) showing OMEGA orbit 41 (L_s 338° in MY 26). (d) Classified image from Piqueux et al. (2008) showing THEMIS temperature data spanning L_s 320°–360°. A hillshade is shown in areas where

THEMIS temperatures are interpreted as neither CO₂ nor H₂O ice. The legend gives best-estimate correlations between spectral properties signified by colors in the different maps.

5.2.2 Characteristics of major units

In the residual ice mosaic, the RCD are mapped primarily as endmember C6m (yellow), indicating CO₂ ice with minor H₂O content (Fig. 8a). However, some areas do show stronger water ice signatures (Fig. 8b) where endmember Cd3m (light green) is mapped around rough erosional morphology and endmembers Dw3m and Dc3m (blue and pink) appear in erosional windows through the RCD. Exposures of the PWD display varying compositions from pure water ice (W1m, deep blue) to more dust (W3m and Dw3m in lighter blues) and even contributions from CO₂ ice (Cw3m, Dc3m in shades of pink). Although water/dust combinations can vary strip-to-strip (e.g., Fig 8c), the outlines of endmember divisions are consistently mapped in these regions. Similarly, the OWD displays a wide variety of compositions such that all 12 endmembers are present (Fig. 8d). These variations closely follow differences in albedo visible in a Mars Orbiter Camera (MOC) mosaic, providing opportunities to study a wealth of contacts between SPLD, OWD, and low-elevation portions of the RCD. Lastly, the SPLD is mapped broadly as endmember Cd1 (pale blue) without the ability to see compositional differences in exposed layers.

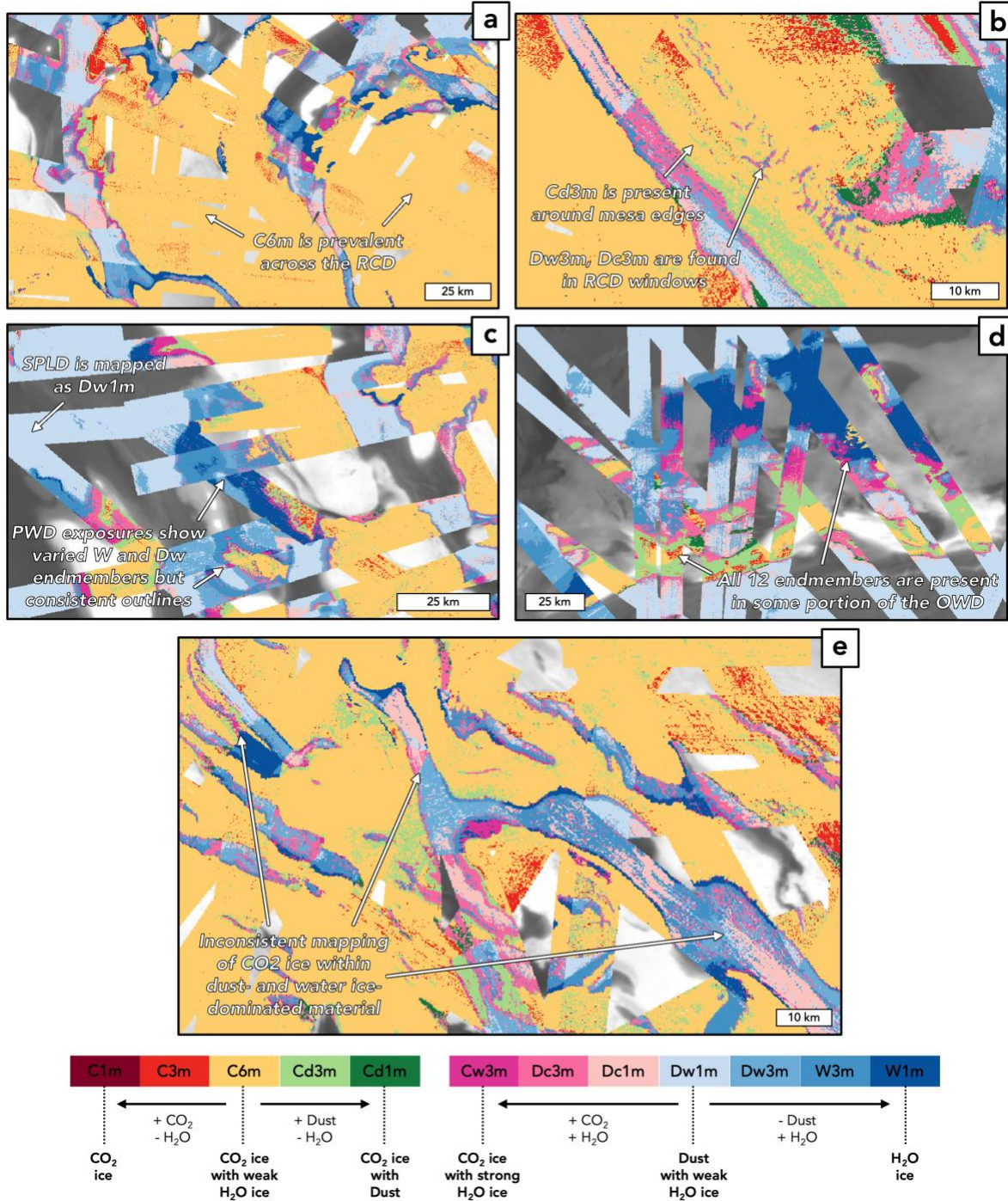


Figure 8. Details of the mosaic showing residual ice surfaces. (a) Portions of the RCD showing agreement in residual CO₂ ice signatures. (b) A portion of the RCD in which compositional details around erosional features are resolved as more water ice-rich endmembers. (c) Exposures of the PWD in which some strips show variable contributions of dust with water ice, but generally follow the same contours on the surface. (d) The OWD showing a wide variety of

endmember mappings. (e) Detail around dark lanes showing inconsistent mapping of CO₂ ice features with water and dust, expressed as alternating pink and blue classifications.

5.2.3 Variable CO₂ ice signatures

Targeted data showed that dark material surrounding the RCD was almost universally mapped with weak CO₂ ice signatures (shades of pink) across L_s and MYs, even after the removal of apparent seasonal frost. The presence of such a consistent signature indicated that residual CO₂ ice of some kind extends beyond the brightest exposures of CO₂ ice and into surrounding dust- or H₂O ice-dominated deposits. This finding suggests a complex stratigraphy in which layered and unlayered low-albedo material usually presumed to be the SPLD includes some amount of CO₂ ice, which could have implications for how material is introduced into climate records. These same CO₂ ice-bearing exposures are captured by the mapping data results, but are less consistently mapped as evidenced by alternating classification between shades of blue (dust/water ice without CO₂) and shades of pink (also dust/water but with weak CO₂ ice features)(Fig. 8e).

The less consistent expression of weak CO₂ ice features in the mapping data classification is likely caused by the dataset's more limited wavelength sampling and increased spatial binning. Additionally, the random forest model might not be sufficiently sensitive to weak signatures that remain at these lower resolutions. Alternatively, actual CO₂ ice contributions on the surface might be more variable than what is captured by targeted data maps: diurnal, intra-annual, and inter-annual variations could all contribute to the observed variation. In particular, local variations in illumination during the extended days of south polar summer could produce shadowed regions where CO₂ ice accumulates. Depending on the timing of the next overlapping observation several L_s or even MYs later, such shadowed regions could be illuminated again.

6. Conclusions

The new endmember-classified mosaics of CRISM mapping data expand on previous compositional mapping of the SPRC to provide new insights into the dynamic processes that shape this region. Our results and interpretations can be summarized as follows:

- A total of 1103 mapping data strips spanning southern summer of MY 28–33 were processed using a combination of *k*-means clustering and random forest classification. The resulting set of 12 endmembers were found to display spectral signatures consistent with the results of Cartwright et al. (2022), allowing a one-to-one comparison of compositional variation captured by CRISM targeted data and mapping data.
- The classified observations were compiled into a series of temporally restricted mosaics that show how surface composition varies within and between MYs. Importantly, these mosaics allow seasonal variation to be measured within bright exposures of residual CO₂ ice, which is not possible with other datasets covering thermal or visible wavelengths. Consistent with the previous targeted data analyses, CO₂ ice-rich endmembers were found to dominate surface spectra in MY 28. Seasonal retreat in the years that followed was markedly different, potentially with subtle contributions from H₂O ice as early as L_s 270°. This suggests that the large dust event in MY 28 caused either a thicker depositing of seasonal CO₂ frost or a reduction in the amount of H₂O ice contributing to that frost cover.

- By identifying Ls ranges within each MY that did not show significant contribution from CO₂ frost, a mosaic was constructed to show spectral signatures of residual ice deposits. The distribution of ice mixtures is largely consistent with previous OMEGA and THEMIS maps (Douté et al., 2007; Piqueux et al., 2008), but the higher spatial and spectral resolution of CRISM mapping data provides critical new detail. In particular, a greater variety of water ice-rich mixtures can be distinguished compared to THEMIS and their exposure can be resolved in greater detail compared to OMEGA.
- Weak CO₂ ice contributions to dust or H₂O ice-rich mixtures outside the bright residual CO₂ deposits were mapped less consistently in the new mosaics compared to targeted data. This is likely due to the limited spatial and spectral resolution of the mapping data and/or limited sensitivity of the random forest model to these weak features. However, the finding might also point to diurnal or inter-annual variation in CO₂ ice contributions to non-RCD material that is not related to intra-annual trends in seasonal frost removal. This emphasizes the dynamic nature of south polar terrains, where subtle but constant shifts in surface composition can be found, even on exposures of residual ice.
- This work provides a compositional framework that can place the results of Cartwright et al. (2022) into a broader spatial context and aid future studies of south polar composition. For example, constraining the nature of observed mixtures may reveal connections to the formation/evolution of climate records while comparisons of overlapping data will help to track these dynamic processes in detail.

Acknowledgments

This work was made possible through the incredible efforts of the CRISM team and was supported by NASA's Mars Data Analysis Program (80NSSC19K0013). The authors thank Mathieu Vincendon and Sylvain Piqueux for insightful comments that greatly improved the quality of the manuscript.

Open Research

CRISM Targeted Reduced Data Records (TRDRs, Version 3) used in this study are publicly available via the Geosciences Node of the Planetary Data System (Murchie, 2006; Seelos et al., 2023). The derived CRISM endmember spectral library and classified maps are available via a Zenodo repository (Cartwright, 2023). Code written for this study used the open-source Python *scikit-learn* and R *randomForest* libraries (Liaw & Wiener, 2002; Pedregosa et al., 2011). Spatial data were viewed in Esri ArcGIS Pro (Esri Inc., 2020), which is license restricted.

References

- Alsaeed, N. R., & Hayne, P. O. (2022). Transport of Water Into the Polar Regions of Mars Through Scavenging by CO₂ Snowfall. *Journal of Geophysical Research: Planets*, 127(11), e2022JE007386. <https://doi.org/10.1029/2022JE007386>
- Appéré, T., Schmitt, B., Langevin, Y., Douté, S., Pommerol, A., Forget, F., Spiga, A., Gondet, B., & Bibring, J.-P. (2011). Winter and spring evolution of northern seasonal deposits on Mars from OMEGA on Mars Express. *Journal of Geophysical Research: Planets*, 116(E5). <https://doi.org/10.1029/2010JE003762>

- Arthur, D., & Vassilvitskii, S. (2007). k-means++: The advantages of careful seeding. *Proceedings of the Eighteenth Annual ACM-SIAM Symposium on Discrete Algorithms*, 1027–1035.
- Bibring, J.-P., Langevin, Y., Poulet, F., Gendrin, A., Gondet, B., Berthé, M., Soufflot, A., Drossart, P., Combes, M., Bellucci, G., Moroz, V., Mangold, N., Schmitt, B., & OMEGA Team, the. (2004). Perennial water ice identified in the south polar cap of Mars. *Nature*, 428(6983), Article 6983. <https://doi.org/10.1038/nature02461>
- Bibring, J.-P., Soufflot, A., Berthé, M., Langevin, Y., Gondet, B., Drossart, P., Bouyé, M., Combes, M., Semery, A., Bellucci, G., Formisano, V., Moroz, V., Kottsov, V., Bonello, G., Erard, S., Forni, O., Gendrin, A., Manaud, N., Poulet, F., ... Forget, F. (n.d.). *OMEGA: Observatoire pour la Minéralogie, l'Eau, les Glaces et l'Activité*. 13.
- Breiman, L. (2001). Random Forests. *Machine Learning*, 45(1), 5–32. <https://doi.org/10.1023/A:1010933404324>
- Brown, A. J., Calvin, W. M., & Murchie, S. L. (2012). Compact Reconnaissance Imaging Spectrometer for Mars (CRISM) north polar springtime recession mapping: First 3 Mars years of observations. *Journal of Geophysical Research: Planets*, 117(E12). <https://doi.org/10.1029/2012JE004113>
- Brown, A. J., Piqueux, S., & Titus, T. N. (2014). Interannual observations and quantification of summertime H₂O ice deposition on the Martian CO₂ ice south polar cap. *Earth and Planetary Science Letters*, 406, 102–109. <https://doi.org/10.1016/j.epsl.2014.08.039>
- Brown, A. J., Calvin, W. M., McGuire, P. C., & Murchie, S. L. (2010). Compact Reconnaissance Imaging Spectrometer for Mars (CRISM) south polar mapping: First Mars year of observations. *Journal of Geophysical Research*, 115, E00D13. <https://doi.org/10.1029/2009JE003333>
- Byrne, S. (2009). The Polar Deposits of Mars. *Annual Review of Earth and Planetary Sciences*, 37(1), 535–560. <https://doi.org/10.1146/annurev.earth.031208.100101>
- Calvin, W. M., Cantor, B. A., & James, P. B. (2017). Interannual and seasonal changes in the south seasonal polar cap of Mars: Observations from MY 28-31 using MARCI. *Icarus*, 292, 144–153. <https://doi.org/10.1016/j.icarus.2017.01.010>
- Cartwright, S. F. A., Calvin, W. M., Seelos, K. D., & Seelos, F. P. (2022). Characterizing Seasonal and Residual Ices at the South Pole of Mars Using a Universal Set of CRISM Spectral Endmembers. *Journal of Geophysical Research: Planets*, 127(11), e2022JE007372. <https://doi.org/10.1029/2022JE007372>
- Cartwright, S. F. A. (2023). Endmember spectra and classified mosaics derived from CRISM mapping data at the south pole of Mars [Data set]. Zenodo. <https://doi.org/10.5281/zenodo.8201616>
- Christensen, P. R., Jakosky, B. M., Kieffer, H. H., Malin, M. C., McSween, H. Y., Nealson, K., Mehall, G. L., Silverman, S. H., Ferry, S., Caplinger, M., & Ravine, M. (2004). The Thermal Emission Imaging System (THEMIS) for the Mars 2001 Odyssey Mission. *Space Science Reviews*, 110(1), 85–130. <https://doi.org/10.1023/B:SPAC.0000021008.16305.94>

- 702 Diniega, S., Bramson, A. M., Buratti, B., Buhler, P., Burr, D. M., Chojnacki, M., Conway, S. J.,
703 Dundas, C. M., Hansen, C. J., McEwen, A. S., Lapôtre, M. G. A., Levy, J., Mc Keown,
704 L., Piqueux, S., Portyankina, G., Swann, C., Titus, T. N., & Widmer, J. M. (2021).
705 Modern Mars' geomorphological activity, driven by wind, frost, and gravity.
706 *Geomorphology*, 380, 107627. <https://doi.org/10.1016/j.geomorph.2021.107627>
- 707 Douté, S., Schmitt, B., Langevin, Y., Bibring, J.-P., Altieri, F., Bellucci, G., Gondet, B., &
708 Poulet, F. (2007). South Pole of Mars: Nature and composition of the icy terrains from
709 Mars Express OMEGA observations. *Planetary and Space Science*, 55(1–2), 113–133.
710 <https://doi.org/10.1016/j.pss.2006.05.035>
- 711 Esri Inc. (2020). ArcGIS Pro Version 2.5 [Software]. Esri Inc. Retrieved
712 from <https://www.esri.com/en-us/arcgis/products/arcgis-pro/overview>
- 713 James, P. B., Thomas, P. C., Wolff, M. J., & Bonev, B. P. (2007). MOC observations of four
714 Mars year variations in the south polar residual cap of Mars. *Icarus*, 192(2), 318–326.
715 <https://doi.org/10.1016/j.icarus.2007.07.014>
- 716 Kieffer, H. H. (1979). Mars south polar spring and summer temperatures: A residual CO₂ frost.
717 *Journal of Geophysical Research: Solid Earth*, 84(B14), 8263–8288.
718 <https://doi.org/10.1029/JB084iB14p08263>
- 719 Landis, M. E., Acharya, P. J., Alsaeed, N. R., Andres, C., Becerra, P., Calvin, W. M., Cangi, E.
720 M., Cartwright, S. F. A., Chaffin, M. S., Diniega, S., Dundas, C. M., Hansen, C. J.,
721 Hayne, P. O., Herkenhoff, K. E., Kass, D. M., Khuller, A. R., McKeown, L. E., Russell,
722 P. S., Smith, I. B., ... Whitten, J. L. (2023). Polar science results from Mars
723 Reconnaissance Orbiter: Multiwavelength, multiyear insights. *Icarus*, 115794.
724 <https://doi.org/10.1016/j.icarus.2023.115794>
- 725 Langevin, Y., Bibring, J.-P., Montmessin, F., Forget, F., Vincendon, M., Douté, S., Poulet, F., &
726 Gondet, B. (2007). Observations of the south seasonal cap of Mars during recession in
727 2004–2006 by the OMEGA visible/near-infrared imaging spectrometer on board Mars
728 Express. *Journal of Geophysical Research: Planets*, 112(E8).
729 <https://doi.org/10.1029/2006JE002841>
- 730 Liaw, A., & Wiener, M. (2002). Classification and regression by randomForest. *R*
731 *News*, 2(3), 18– 22. Retrieved from <https://CRAN.R-project.org/doc/Rnews/>
- 732 Murchie, S. (2006). *MRO CRISM TARGETED REDUCED DATA RECORD V1.0* [Data set].
733 NASA Planetary Data System. <https://doi.org/10.17189/1519450>
- 734 Murchie, S., Guinness, E., and Slavney, S. (2016). CRISM Data Product Software Interface
735 Specification, Version 1.3.7.4. [https://pds-geosciences.wustl.edu/mro/mro-m-crism-2-](https://pds-geosciences.wustl.edu/mro/mro-m-crism-2-edr-v1/mrocr_0001/document/crism_dpsis.pdf)
736 [edr-v1/mrocr_0001/document/crism_dpsis.pdf](https://pds-geosciences.wustl.edu/mro/mro-m-crism-2-edr-v1/mrocr_0001/document/crism_dpsis.pdf)
- 737 Murchie, S., Arvidson, R., Bedini, P., Beisser, K., Bibring, J.-P., Bishop, J., Boldt, J., Cavender,
738 P., Choo, T., Clancy, R. T., Darlington, E. H., Des Marais, D., Espiritu, R., Fort, D.,
739 Green, R., Guinness, E., Hayes, J., Hash, C., Heffernan, K., ... Wolff, M. (2007).
740 Compact Reconnaissance Imaging Spectrometer for Mars (CRISM) on Mars
741 Reconnaissance Orbiter (MRO). *Journal of Geophysical Research*, 112(E5), E05S03.
742 <https://doi.org/10.1029/2006JE002682>

- Murray, B. C., Soderblom, L. A., Cutts, J. A., Sharp, R. P., Milton, D. J., & Leighton, R. B. (1972). Geological framework of the south polar region of Mars. *Icarus*, 17(2), 328–345. [https://doi.org/10.1016/0019-1035\(72\)90004-8](https://doi.org/10.1016/0019-1035(72)90004-8)
- Pedregosa, F., Varoquaux, G., Gramfort, A., Michel, V., Thirion, B., Grisel, O., Blondel, M., Prettenhofer, P., Weiss, R., Dubourg, V., Vanderplas, J., Passos, A., Cournapeau, D., Brucher, M., Perrot, M., & Duchesnay, É. (2011). Scikit-learn: Machine Learning in Python. *The Journal of Machine Learning Research*, 12(null), 2825–2830.
- Piqueux, S., Byrne, S., Kieffer, H. H., Titus, T. N., & Hansen, C. J. (2015). Enumeration of Mars years and seasons since the beginning of telescopic exploration. *Icarus*, 251, 332–338. <https://doi.org/10.1016/j.icarus.2014.12.014>
- Piqueux, S., Edwards, C. S., & Christensen, P. R. (2008). Distribution of the ices exposed near the south pole of Mars using Thermal Emission Imaging System (THEMIS) temperature measurements. *Journal of Geophysical Research: Planets*, 113(E8). <https://doi.org/10.1029/2007JE003055>
- Piqueux, S., Kleinböhl, A., Hayne, P. O., Kass, D. M., Schofield, J. T., & McCleese, D. J. (2015). Variability of the martian seasonal CO₂ cap extent over eight Mars Years. *Icarus*, 251, 164–180. <https://doi.org/10.1016/j.icarus.2014.10.045>
- Plaut, J. J., Picardi, G., Safaeinili, A., Ivanov, A. B., Milkovich, S. M., Cicchetti, A., Kofman, W., Mouginot, J., Farrell, W. M., Phillips, R. J., Clifford, S. M., Frigeri, A., Orosei, R., Federico, C., Williams, I. P., Gurnett, D. A., Nielsen, E., Hagfors, T., Heggy, E., ... Edenhofer, P. (2007). Subsurface Radar Sounding of the South Polar Layered Deposits of Mars. *Science*, 316(5821), 92–95. <https://doi.org/10.1126/science.1139672>
- Prettyman, T. H., Feldman, W. C., & Titus, T. N. (2009). Characterization of Mars’ seasonal caps using neutron spectroscopy. *Journal of Geophysical Research: Planets*, 114(E8). <https://doi.org/10.1029/2008JE003275>
- Seelos, F. P., Seelos, K. D., Murchie, S. L., Novak, M. A. M., Hash, C. D., Morgan, M. F., Arvidson, R. E., Aiello, J., Bibring, J.-P., Bishop, J. L., Boldt, J. D., Boyd, A. R., Buczkowski, D. L., Chen, P. Y., Clancy, R. T., Ehlmann, B. L., Frizzell, K., Hancock, K. M., Hayes, J. R., ... Wolff, M. J. (2023). The CRISM investigation in Mars orbit: Overview, history, and delivered data products. *Icarus*, 115612. <https://doi.org/10.1016/j.icarus.2023.115612>
- Smith, I. B. (2022). A Retrospective on Mars Polar Ice and Climate. In I. B. Smith, *Oxford Research Encyclopedia of Planetary Science*. Oxford University Press. <https://doi.org/10.1093/acrefore/9780190647926.013.242>
- Thomas, P. C., Calvin, W., Cantor, B., Haberle, R., James, P. B., & Lee, S. W. (2016). Mass balance of Mars’ residual south polar cap from CTX images and other data. *Icarus*, 268, 118–130. <https://doi.org/10.1016/j.icarus.2015.12.038>
- Thomas, P. C., Malin, M. C., Edgett, K. S., Carr, M. H., Hartmann, W. K., Ingersoll, A. P., James, P. B., Soderblom, L. A., Veverka, J., & Sullivan, R. (2000). North–south geological differences between the residual polar caps on Mars. *Nature*, 404(6774), Article 6774. <https://doi.org/10.1038/35004528>

- 784 Titus, T. N., Kieffer, H. H., & Christensen, P. R. (2003). Exposed Water Ice Discovered near the
785 South Pole of Mars. *Science*, 299(5609), 1048–1051.
786 <https://doi.org/10.1126/science.1080497>
- 787 Titus, T. N., Williams, K. E., & Cushing, G. E. (2020). Conceptual Model for the Removal of
788 Cold-Trapped H₂O Ice on the Mars Northern Seasonal Springtime Polar Cap.
789 *Geophysical Research Letters*, 47(15), e2020GL087387.
790 <https://doi.org/10.1029/2020GL087387>
- 791 Viviano, C. E., Seelos, K. D., Phillips, M. S., Cartwright, S. F. A., Beck, A. W., Seelos, F. P.,
792 Murchie, S. L., Dapremont, A. M., Frizzell, K. R., & Smith, I. B. (2020). *Regional*
793 *compositional mapping using CRISM multispectral mapping data*. 51st Lunar and
794 Planetary Science Conference, Houston, TX.
795 <https://www.hou.usra.edu/meetings/lpsc2020/pdf/1485.pdf>
- 796 Viviano-Beck, C. E., Seelos, F. P., Murchie, S. L., Kahn, E. G., Seelos, K. D., Taylor, H. W.,
797 Taylor, K., Ehlmann, B. L., Wiseman, S. M., Mustard, J. F., & Morgan, M. F. (2014).
798 Revised CRISM spectral parameters and summary products based on the currently
799 detected mineral diversity on Mars: REVISED CRISM SUMMARY PRODUCTS.
800 *Journal of Geophysical Research: Planets*, 119(6), 1403–1431.
801 <https://doi.org/10.1002/2014JE004627>
- 802 Wagstaff, K. L., Titus, T. N., Ivanov, A. B., Castaño, R., & Bandfield, J. L. (2008). Observations
803 of the north polar water ice annulus on Mars using THEMIS and TES. *Planetary and*
804 *Space Science*, 56(2), 256–265. <https://doi.org/10.1016/j.pss.2007.08.008>

Spatial and Temporal Variation of Mars South Polar Ice Composition from Spectral Endmember Classification of CRISM Mapping Data

S. F. A. Cartwright^{1,2}, W. M. Calvin³, K. D. Seelos², and F. P. Seelos²

¹Department of Geological Sciences, Laboratory for Atmospheric and Space Physics, University of Colorado, Boulder, CO, USA, ²Johns Hopkins University Applied Physics Laboratory, Laurel, MD, USA, ³Department of Geological Sciences and Engineering, University of Nevada, Reno, NV, USA

Contents of this file

Text S1

Figures S1 to S3

Introduction

The text description and three figures included in this file provide additional context for the process of deriving the final endmembers presented in the main text. Specifically, they detail how the original targeted data endmember set from Cartwright et al. (2022)(Fig. S1a) was subsampled to mapping data wavelengths (Fig. S1b), how those endmembers were combined to make 13 reference spectra (Fig. S2a), and how candidate endmembers from the mapping dataset were assigned to those reference spectra (Fig. S2b). A comparison of spectral feature strength between mapping and targeted endmembers is also presented (Fig. S3).

Text S1.

As described in Section 3 of the main text, south polar CRISM mapping data were processed with *k*-means clustering and random forest classification to extract a set of 30 candidate spectral endmembers. These endmembers characterize the diversity of spectral variation present in the mapping dataset. In Cartwright et al. (2022), we used similar processing techniques to derive a set of 21 spectral endmembers that characterize the diversity of spectral variation present in the CRISM targeted dataset. To compare the results of these two investigations, it was necessary to assign each of the

new candidate mapping endmembers to an appropriate endmember identified with targeted data. This process is outlined in Figure 2 in the main text and elaborated below.

To enable a more direct comparison of the spectral structures captured in both datasets, we first downsampled the original 21 targeted endmembers (Fig. S1a) from their original 438 shortwave-infrared channels to the set of 55 sampled in mapping data (Fig. S1b). However, this process removed or subdued spectral differences present in the suite of 21 targeted endmembers, meaning that some of the downsampled spectra were no longer meaningfully separable. We therefore found it necessary to combine some endmembers in a process illustrated in Figure S2a. This combination process produced a collection of 13 reference spectra to which the 30 candidate mapping data endmembers could be compared.

The 13 reference spectra still capture the range of spectral diversity present in the original targeted endmember set, but without the resolution needed to separate some pairings within compositional gradations. In general, we found that the endpoints of the gradations remained distinct (e.g., Dc1 and Dc3), but that intermediate endmembers (e.g., Dc2) could be combined with one endpoint or the other.

To assign candidate endmembers, we visually compared the spectra of a given candidate to all 13 reference spectra and determined which pairing had the most similar spectral structure (i.e., strengths and combinations of CO₂ and H₂O ice absorptions). Where this spectral assignment was ambiguous, we looked at the endmember distribution in classified mapping data mosaics. The final endmember assignments for each of the 30 candidates is visualized in Figure S2b.

Of the 13 reference spectra, 12 of them were found to be present in the mapping data results from random forest classification. Only one reference endmember (Cw1) was not found to have an equivalent in the mapping dataset; see the main text for possible explanations of this absence. Additionally, some CO₂ ice-rich endmembers and three apparent error modes (see Fig. S2b) were difficult to assign based on spectral features alone so they were isolated in mosaics and assigned based on spatial correlation with other endmembers.

The result of this process was a reassignment scheme used to reclassify the random forest results. This produced a final set of 12 mapping data endmembers and a collection of endmember-classified maps directly linked to the compositional framework described in Cartwright et al. (2022).

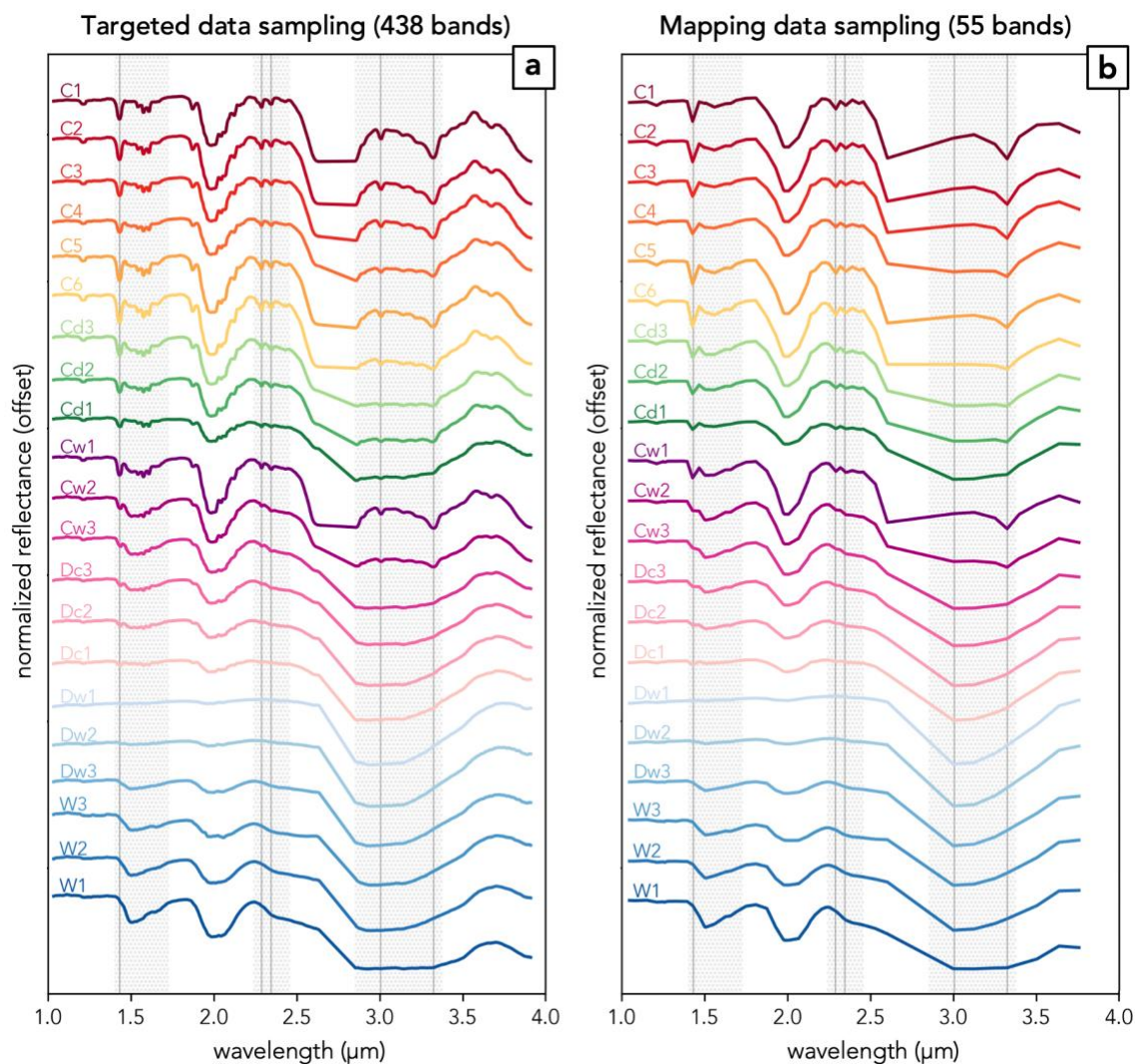


Figure S1. (a) The endmember set presented in Cartwright et al. (2022) derived from CRISM targeted data at the full spectral resolution of 438 SWIR channels. (b) The same endmembers when subsampled to the 55 spectral channels present in MSP and MSW data. Due to the removal of consistently suspect spectral channels, the actual band counts for targeted and mapping data used in these studies is 404 and 51, respectively. In both plots, vertical lines indicate narrow absorption features associated with CO₂ ice while hatched regions mark the bounds of broader absorptions associated with H₂O ice.

Note that even weaker expressions of each of these key features at full resolution are still visible in the subsampled set. A major exception is the region around 2.9–3.4 μm .

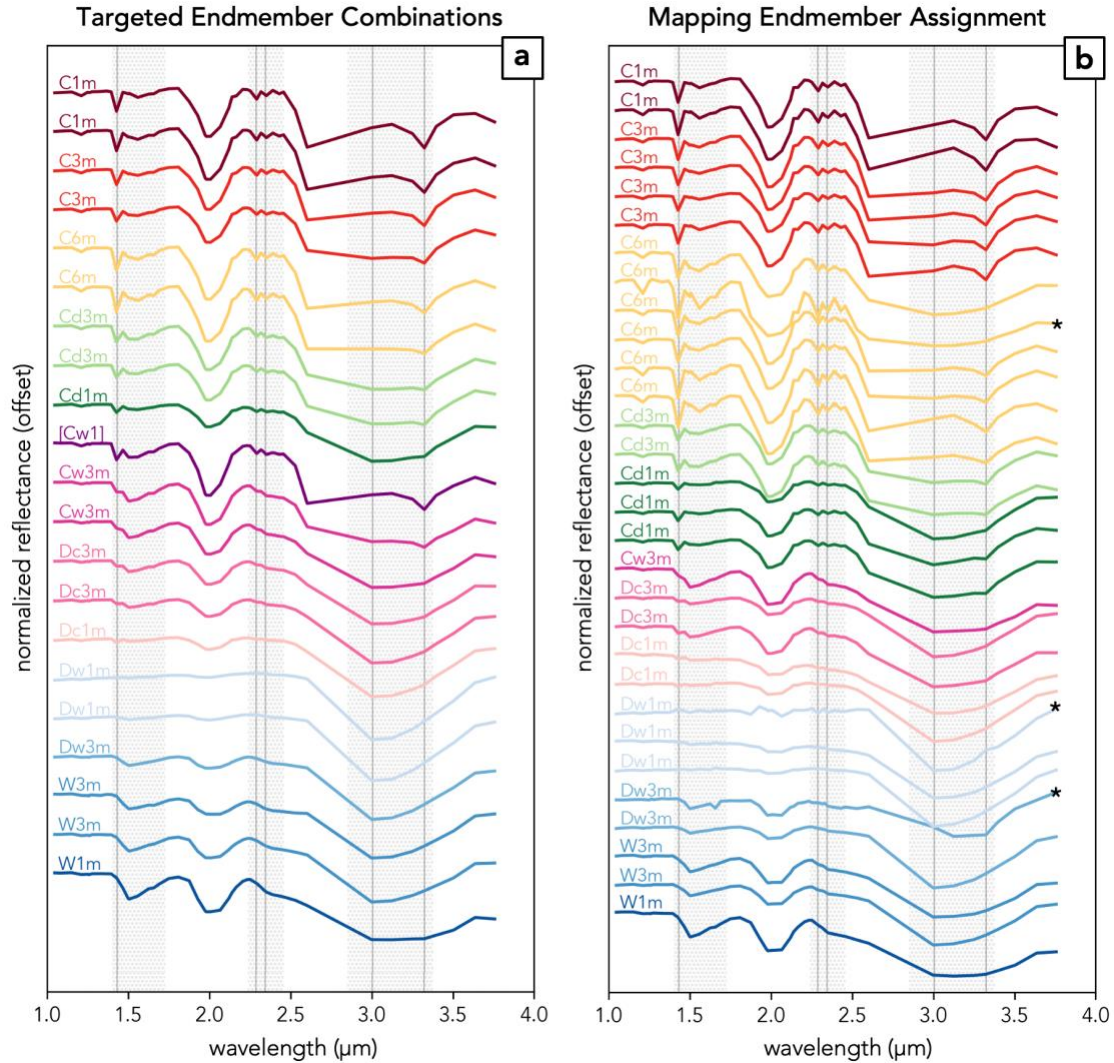


Figure S2. (a) The subsampled endmembers from Cartwright et al. (2022) colored and labeled according to how they were combined to create the 13 reference endmembers. Note the broad similarities in feature combinations and strengths between pairs that share the same color. Endmember Cw1 is also included here, though it was not found to be comparable to any of the candidate endmembers identified in CRISM mapping data. (b) The 30 candidate endmembers identified in mapping data colored and labeled according to which of the final 12 endmembers they were assigned to. Asterisks at the far right mark three endmembers associated with apparent error modes, which are expressed as noisy or otherwise unusually shaped spectra; these were assigned to an endmember based on spatial association with other endmembers in classified mosaics. Note that the six endmembers reclassified to C6m have consistently strong $\sim 1.6 \mu\text{m}$ features that distinguish them from endmembers reclassified to C1m and C3m, but that

there are subtle differences in 1.5 μm feature strength that reflect the amount of water ice present.

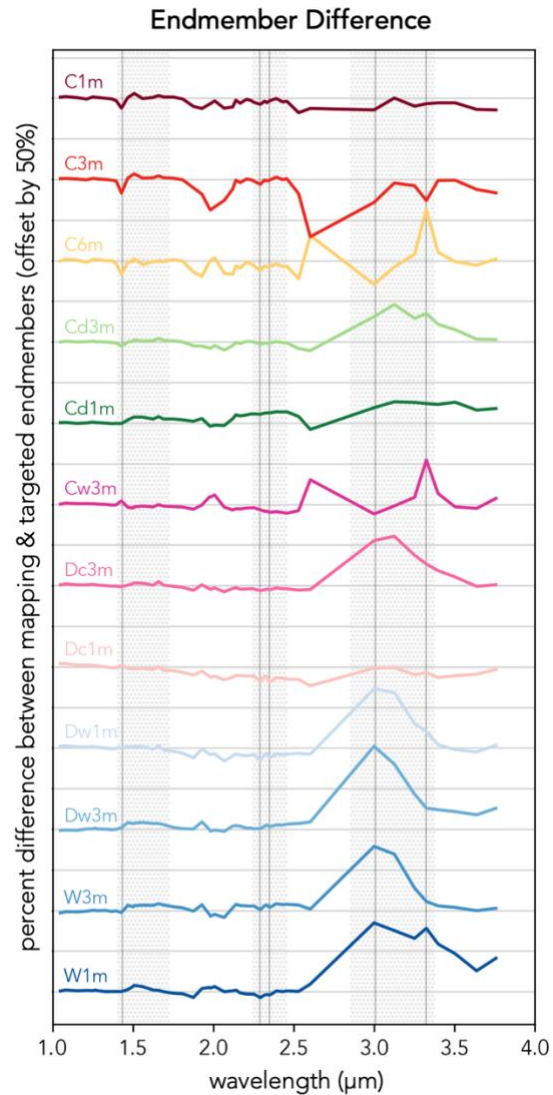


Figure S3. Plot of the percent difference between the mapping data endmembers shown in Figure 3 in the main text and the corresponding spectra for subsampled targeted data endmembers. Spectra are offset in 50% intervals and horizontal lines mark each 25% interval. Vertical lines mark narrow CO₂ ice features while hatched regions mark broad H₂O ice absorptions. Features that appear to jut above the continuum represent places where spectral features are weaker in mapping data while those that point downward indicate stronger features in mapping data. Pronounced differences at long wavelengths can be attributed to the CRISM filter boundary and suspect radiometry. In general, mapping data endmembers have stronger CO₂ ice features in CO₂ ice-dominated spectra, but weaker H₂O ice features in H₂O ice-dominated spectra compared to the corresponding targeted endmember.